ACCOUNTS
of chemical research

Controlling the Band Gap Energy of Cluster-Assembled Materials

SUKHENDU MANDAL,[†,⊥,∥] ARTHUR C. REBER,[‡,⊥] MEICHUN QIAN,[‡] PAUL S. WEISS,[*,†,§] SHIV N. KHANNA,[*,‡] AND AYUSMAN SEN[*,†]

[†]*Department of Chemistry, The Pennsylvania State University, University Park, Pennsylvania 16802, United States,* [‡]*Department of Physics, Virginia Commonwealth University, Richmond, Virginia 23284, United States, and* [§]*California NanoSystems Institute, Departments of Chemistry & Biochemistry and Materials Science & Engineering, University of California, Los Angeles, Los Angeles, California 90095, United States*

RECEIVED ON OCTOBER 29, 2012

CONSPECTUS

Cluster-assembled materials combine the nanoscale size and composition-dependent properties of clusters, which have highly tunable magnetic and electronic properties useful for a great variety of potential technologies. To understand the emergent properties as clusters are assembled into hierarchical materials, we have synthesized 23 cluster-assembled materials composed of As_7^{3-}-based motifs and different countercations and measured their band gap energies. We found that the band gap energy varies from 1.09 to 2.21 eV. In addition, we have carried out first principles electronic structure studies to identify the physical mechanisms that enable control of the band gap edges of the cluster assemblies.

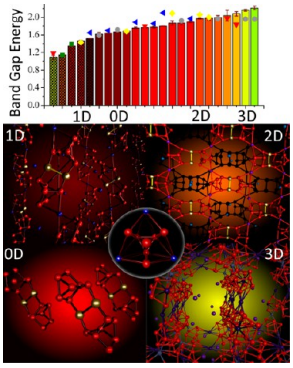

The choice of counterion has a profound effect on the band gap energy in ionic cluster assemblies. The top of the valence band is localized on the arsenic cluster, while the conduction band edge is located on the alkali metal counterions. Changing the counterion changes the position of the conduction band edge, enabling control of the band gap energy. We can also vary the architecture of the ionic solid by incorporating cryptates as counterions, which provide charge but are separated from the clusters by bulky ligands. Higher dimensionality typically decreases the band gap energy through band broadening; however band gap energies increased upon moving from zero-dimensional (0D) to two-dimensional (2D) assemblies. This is because internal electric fields generated by the counterion preferentially stabilize the adjacent lone pair orbitals that mark the top of the valence band. Thus, the choice of the counterion can control the position of the conduction band edge of ionic cluster assemblies. In addition, the dimensionality of the solid via internal electric fields can control the valence band edge.

Through covalently linking arsenic clusters into composite building blocks, we have also been able to tune the band gap energy. We used a theoretical description based on cluster orbital theory to provide microscopic understanding of the electronic character of the composite building blocks and the observed variations in the band gap energy. Also, we have shown how dimeric linkers can be used to control the band gap energy. Lastly, we also investigated the effects of charge transfer complexes of $M(CO)_3$ on the band gap energy.

Introduction

Materials in which nanoscale clusters serve as building blocks enable the integration of multiple length scales into a hierarchical material.[1,2] Since the properties of clusters change with size, composition, and oxidation state, and the emergent behaviors depend on their architecture, cluster assemblies offer the attractive proposition of forming materials with novel combinations of properties. These materials serve as links between the predictable size-invariant properties of solids and the evolution in properties observed at the subnanometer scale where every atom and every electron count.[3−12] Recent synthetic advances confirm that the materials retain many of the characteristics of the original building blocks.[13−15] Cluster-assembled solids involve building motifs coupled by linkers and offer unusual properties because they combine intracluster, intercluster,

Published on the Web 06/04/2013 www.pubs.acs.org/accounts
10.1021/ar3002975

and linker-cluster interactions, unavailable in atomic solids.[16−20] The fundamental question is, what controls the properties once the clusters are incorporated into an extended nanoscale material?

An important class of cluster-assembled solids are the Zintl phases where the primitive motifs are the multiply charged polyatomic anions, called Zintl anions, formed by the heavier (and mildly electronegative) post-transition elements.[1,2] Zintl anions can combine with cations of highly electropositive elements, such as alkali metals, to form crystalline solids and "melts", which are usually referred to as Zintl phases.[2] While Zintl phases have been known for quite some time, recent studies have indicated that the Zintl anions can be covalently linked to make new building blocks and that the nature of the assemblies can be further controlled by extending the countercations to include cryptated ions.[2,21,22] Through variations of the anionic motifs and alkali/cryptated ions, it has become possible to assemble the resulting solids in various architectures including zero-dimensional (0D), one-dimensional (1D), two-dimensional (2D), and three-dimensional (3D) solids. We have synthesized multiple architectures incorporating As_7^{3-} clusters through control of the countercations, variation of the ionic and covalent linker, and addition of charge-transfer complexes. Taking the band gap energy of the resulting material as the property of choice, we demonstrate that the energy bands in these cluster solids exhibit far less dispersion than in atomic solids and that the band gap energy can be controlled over a wide range.

The purpose of this Account is to highlight how the cluster-assembled materials can offer the ability to control band gap energy and provide nanoscopic understanding of such variations. We focus on the cluster-assembled materials derived from anionic As_7^{3-} combined with countercations including alkali metals and cryptated K^+ ions, and building motifs that involve Zintl ions covalently linked with Hg, Zn, Cd, Pd, etc. We first demonstrate how different cluster assemblies can be synthesized by using covalent linkers and assembling them with countercations in various proportions. Through X-ray diffraction, we probe the structures of the new assemblies, and through reflectance spectroscopy, we show how such assemblies offer variations in the band gap energy (Figure 1 and Table 1). First principles electronic structure calculations then probe the nature of the electronic states and, in particular, the nature of electronic orbitals controlling the band edges. The variations in the band gap energy are then shown to result from three distinct effects: (1) the variations in conduction band edge through the choice of countercations, (2) the variations in valence band edge through large ionic fields derived from countercations, and (3) introduction of states in the gap resulting in new band edges much like the impurity states. The first principles studies also demonstrate how the electronic structure of the solids result from the interaction of electronic orbitals of individual clusters and how a basis set consisting of states in individual clusters provides a reasonable framework to analyze the electronic structure of the assembled material. Our studies offer fundamental insights needed to lay the groundwork for the synthesis of new nanoscale materials with tailored properties.

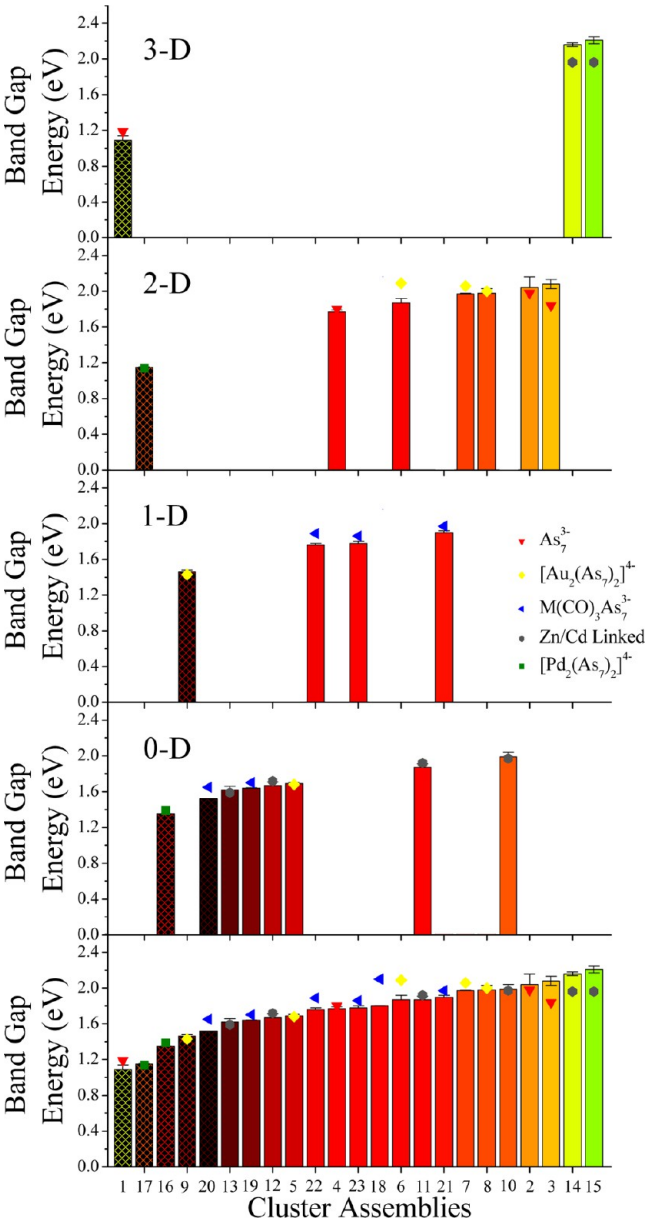

FIGURE 1. Experimental and theoretical band gap energies for 23 cluster-assembled materials. The bar graph and symbols indicate the experimental and theoretical band gap energies. The numbering corresponds to Table 1. The symbol indicates the class of arsenic-based cluster used in the assembly.

TABLE 1. Experimentally Measured and Theoretically Calculated Band Gap Energy for All Clusters

compounds	cluster formula	band gap (eV) (exptl)	band gap (eV) (theor)
1	$[Cs_3][As_7]$	1.09 ± 0.05	1.19
2	$[(K\text{-crypt})Cs_2][As_7]$	2.04 ± 0.17	1.98
3	$[(K\text{-crypt})_{1.5}Cs_{1.5}][As_7]$	2.08 ± 0.05	1.84
4	$[(Rb\text{-crypt})_{1.5}Cs_{1.5}][As_7]$	1.77 ± 0.05	1.80
5	$[K\text{-crypt}]_4[Au_2(As_7)_2]$	1.69 ± 0.02	1.68
6	$[(Rb\text{-crypt})Rb_2]_2[Au_2(As_7)_2]$	1.87 ± 0.05	2.09
7	$[(K\text{-crypt})_2Cs_2][Au_2(As_7)_2]$	1.97 ± 0.01	2.06
8	$[(Rb\text{-crypt})_2Cs_2][Au_2(As_7)_2]$	1.98 ± 0.05	2.00
9	$[(K\text{-crypt})_2K_2][Au_2(As_7)_2]$	1.46 ± 0.02	1.43
10	$[K\text{-crypt}]_4[Zn(As_7)_2]$	1.99 ± 0.05	1.97
11	$[K\text{-crypt}]_4[Cd(As_7)_2]$	1.87 ± 0.04	1.92
12	$[K\text{-crypt}]_4[Hg_2(As_7)_2]$	1.67 ± 0.04	1.72
13	$[K\text{-crypt}]_3[HgAs(As_7)_2]$	1.62 ± 0.04	1.59
14	$[K\text{-crypt}]_2[Zn(As_7)_2Cs_2]$	2.16 ± 0.02	1.96
15	$[K\text{-crypt}]_2[Cd(As_7)_2Rb_2]$	2.21 ± 0.04	1.96
16	$[K\text{-crypt}]_4[Pd_2(As_7)_2]$	1.35 ± 0.003	1.39
17	$[K\text{-crypt}]_2[Pd_2(As_7)_2Cs_2]$	1.15 ± 0.004	1.14
18	$[K\text{-crypt}]_3[Cr(CO)_3As_7]$	1.80 ± 0.003	2.10
19	$[K\text{-crypt}]_3[(en)Mo(CO)_3As_7Mo(CO)_3]$	1.64 ± 0.004	1.70
20	$[K\text{-crypt}]_3[(en)W(CO)_3As_7W(CO)_3]$	1.52 ± 0.004	1.65
21	$[K\text{-crypt}]_2[As_7Cr(CO)_3Cs]$	1.90 ± 0.02	1.97
22	$[K\text{-crypt}]_2[As_7Mo(CO)_3Cs]$	1.76 ± 0.02	1.89
23	$[K\text{-crypt}]_2[As_7W(CO)_3Cs]$	1.78 ± 0.02	1.86

Synthesis and Control of Dimensionality of Cluster-Assembled Materials

Controlling the assembly of multiply charged cluster building blocks into extended solids offers a strategy for constructing ionic cluster-assembled materials with tunable properties. The As_7 cluster typically requires three additional electrons to complete its electronic shell. Numerous cluster solids were crystallized in presence of the polycyclic multidentate ligand, 4,7,13,16,21,24-hexaoxa-1,10-diazabicyclo[8.8.8]hexacosane (known as cryptand-222; henceforth "crypt"), and structurally characterized using X-ray crystallography. The selection of crypt as a cation sequestering agent facilitates the syntheses of Cs-linked cluster assemblies due to crypt's selective sequestering ability for K and Rb over Cs. Figure 2 shows eight cluster-assembled materials, with two examples each of 0D, 1D, 2D, and 3D cluster assemblies. The structural determination by the single-crystal X-ray diffraction technique has been discussed in detail in ref 23. Judicious choice of the counterion, stoichiometry, and degree of cryptation offer several degrees of freedom, which enable the formation of numerous cluster-assembled materials with different properties.

Determination of Band Gap Energy

Variations in the composition and architecture of cluster assemblies constructed from the same building blocks can lead to different optical properties. We demonstrated this by measuring the optical band gap energy of 23 cluster-assembled materials based on As_7 using diffuse reflectance spectroscopy and the Kubelka–Munk model.[24−26] For a crystalline solid with a non-zero band gap energy (E_{bg}), the frequency dependence (ν) of the absorption coefficient (κ) can be approximated as

$$\kappa(\nu) = \frac{B_T(h\nu - E_{bg})^n}{h\nu}$$

where B_T is a constant derived from the square of the averaged dipolar momentum matrix element and n is equal to 0.5 and 2 for *direct* and *indirect* band gap transitions, respectively.[27−29] The absorption coefficient (κ) can be measured from the reflectance (R) and expressed as $\kappa = (1 - R)^2/(2R)$. From the above equation, the band gap energy of a material can be obtained by extrapolating to the x-axis intercept with a linear fit to a plot of $(\kappa h\nu)^{1/n}$ vs $h\nu$. Figure 3A shows these Tauc plots for the measured cluster assemblies **1**−**4**, while the values of the band gap energies for all the mentioned cluster assemblies are plotted in Figure 1 and listed in Table 1. Figure 1 also diagrams the band gap energy of the cluster assemblies as a function of the dimensionality. The results reveal a trend of band gap energies increasing from 0D to higher dimensionalities, although exceptions to this simple rule are observed. The formula for indirect band gap energy was used in all cases as we have found this to be most applicable to these systems with rather flat bands.[23]

Band Gap Energy Tuning: Role of Countercation

We observed significant variations in the band gap energies of cluster-assembled materials constructed from the same As_7^{3-} cluster building block with different countercations.[23]

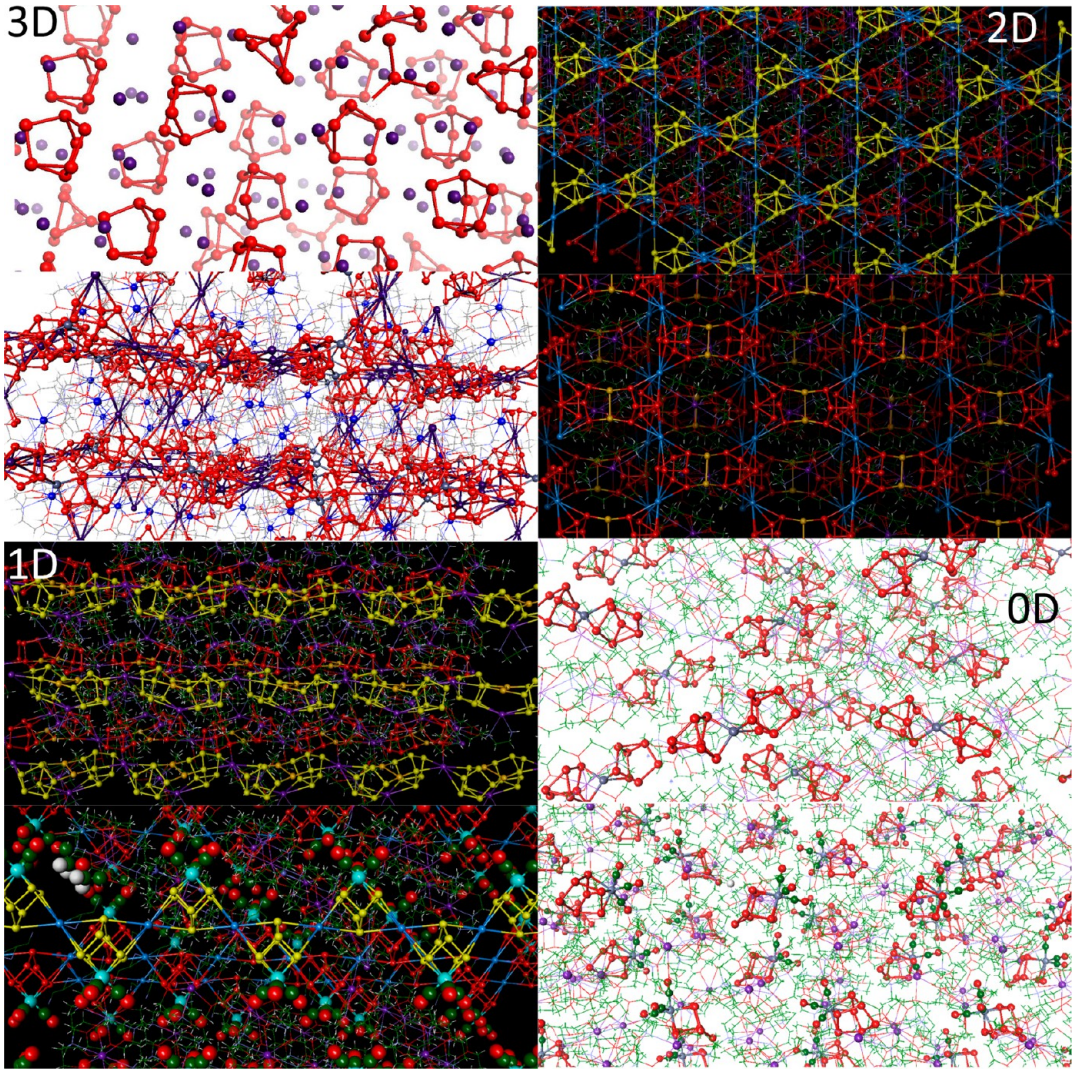

FIGURE 2. Crystal structure of cluster assemblies with 3D architectures (**1** and **14**); 2D architectures (**2** and **7**); 1D architectures (**9** and **23**); and 0D architectures (**10** and **18**).

For example, $[Cs_3][As_7]$ (compound **1**, Figure 2 (3D)) has $E_{bg} =$ 1.09 eV, while $[Cs_2(K\text{-crypt})][As_7]$ (compound **2**, Figure 2 (2D)) has $E_{bg} = 2.04$ eV. Cluster assemblies made from the same motif should be isoelectronic, yet the band gap is almost doubled when Cs is replaced with cryptated K.

First principles electronic structure investigations were undertaken to probe the electronic band structure and the nature of the electronic states marking the set of highest occupied and lowest unoccupied molecular orbitals (HOMO and LUMO, respectively). The calculations on the bulk solids have been performed on the basis of X-ray crystallographic structures. In selected cases, we allowed the structures to relax, but the relaxations were minimal. Consequently, we have used geometries based on experimental X-ray data.

To probe the origins of the variation in the band gap energies, we examined the nature of the frontier orbitals in isolated A_3As_7 clusters. The HOMO and LUMO charge densities are plotted in Figure 3b. The HOMO is composed of contributions from the As atoms, and the LUMO is localized on the alkali metal cations. Further, the LUMO of the material is derived from the absolute position of the HOMO of the neutral alkali metal atom. This close correlation is seen in Figure 3d, which shows the energies of the HOMOs of the alkali metal atoms and the calculated band gap energy of the pure Zintl materials. These were obtained by calculating the band structures of optimized A_3As_7 and A_3As_{11} assemblies for various alkali atoms in the observed orthorhombic and monoclinic structures of Cs_3As_7 and Cs_3As_{11}. The experimental and theoretical band gap energy for $[K\text{-crypt}]_3[As_{11}]$ are also included. The HOMO of the free neutral atom is lowest for lithium and increases as the size of the atom increases, except for the cryptated potassium, in which the

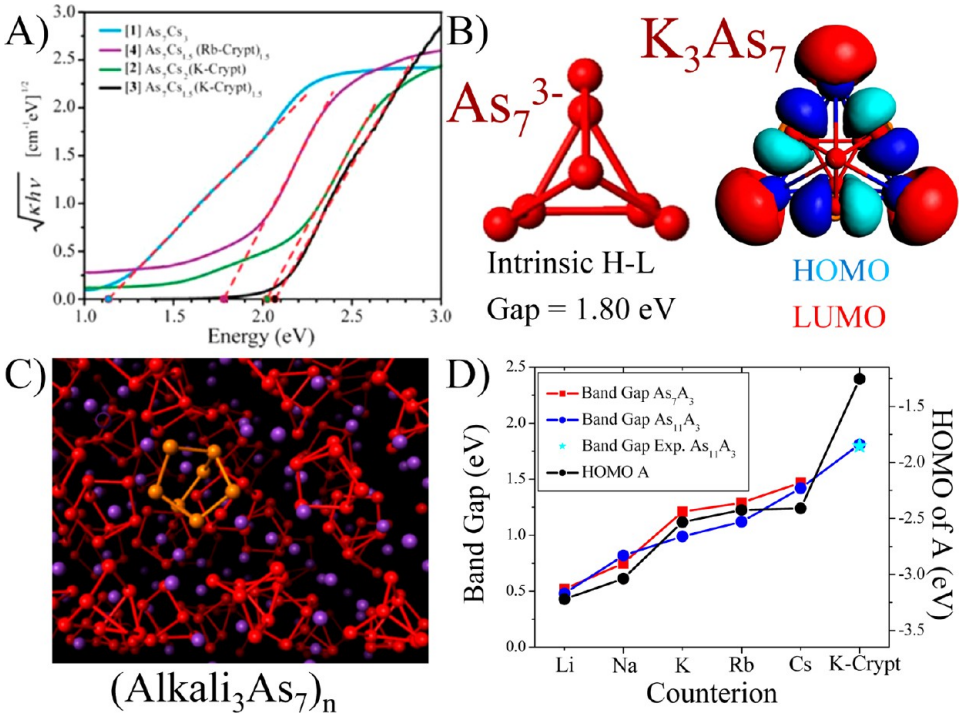

FIGURE 3. (A) Tauc plots of **1**, **2**, **3**, and **4**. (B) Structure of As_7^{3-} and K_3As_7, with frontier orbitals for K_3As_7. (C) Three-dimensional material for $[Cs_3][As_7]$ (compound **1**). (D) Calculated band gap energies for A_3As_7, A_3As_{11}, and $(K\text{-crypt})_3As_{11}$, and the absolute position of the HOMOs of the neutral atoms.

lone pair on the polyether greatly destabilizes the HOMO. Mixing of the states is evident in solids containing multiple countercations, because replacing a single Cs atom with cryptated K ions results in an increase of E_{bg} from 1.1 to 2.1 eV. The nature of the countercation is the dominant factor that controls the band gap energy in these assemblies.

Band Gap Energy Tuning: Role of Internal Electric Field

The HOMO–LUMO gap of the isolated $[As_7]^{3-}$ cluster is 1.80 eV; however, the band gap energy of the 2D sheets of $[As_7]^{3-}$ linked by Cs and Rb and separated by K-crypt are consistently larger, ranging from 1.97 to 2.08 eV. Changing the assembly from a 0D to a 2D architecture is generally expected to decrease the band gap energy through increased band broadening due to larger coordination; however, we generally observe an increase in band gap energy, as seen in Figure 1.[30] The symbols in Figure 1 mark the character of the cluster building block, and the gold-linked, Zn- and Cd-linked, and $M(CO)_3$-bound clusters all show an increase in the band gap energy as the dimensionality of the assembly increases. To understand this phenomenon, we focused our search on the $[Au_2(As_7)_2]^{4-}$ composite cluster in which we synthesized multiple counterion-directed architectures of $[K\text{-crypt}]_4[Au_2(As_7)_2]$ (compound **5**), $[(Rb\text{-crypt})Rb_2]_2[Au_2(As_7)_2]$ (compound **6**), $[(K\text{-crypt})Cs_2]_2[Au_2(As_7)_2]$ (compound **7**), and $[(Rb\text{-crypt})Cs_2]_2[Au_2(As_7)_2]$ (compound **8**).[30] Structural analyses reveal that all these compounds **5**–**8** have the same basic building block $[As_7Au_2As_7]^{4-}$, but changing the cation results in 0D (**5**) and 2D (**6**–**8**) architectures (Figure 4). The experimental band gap energy of compound **5** is found to be 1.69 eV and is in good agreement with the theoretically calculated value of 1.68 eV (Table 1). In this solid, the valence and conduction band edges are derived from As and Au states, respectively, because the K-crypt states are pushed up and buried deep into the conduction band (Figure S2, Supporting Information). The 0D compound **5** reveals the intrinsic band gap energy of an isolated $[Au_2(As_7)_2]^{4-}$ motif and can be used as a guide to understand variations in band gap energies in assemblies with higher connectivity. The structures of **6**–**8** are 2D layers formed by interactions of Rb (**6**) and Cs (**7** and **8**) cations with $[Au_2(As_7)_2]^{4-}$, while cryptated alkali cations separate these layers (Figure 4b and Figures S3 and S4, Supporting Information). The band gap energies of compounds **6**–**8** are found to be 1.87, 1.97, and 1.98 eV, respectively, and are in good agreement with the theoretically calculated values (Table 1). The band gap energies for all of the 2D assemblies (**6**–**8**) are larger than the band gap energy of the 0D assembly (**5**), whose band gap energy is expected to be the upper limit.

How does varying the architecture of the assembly increase the band gap energy to a larger value than that of an

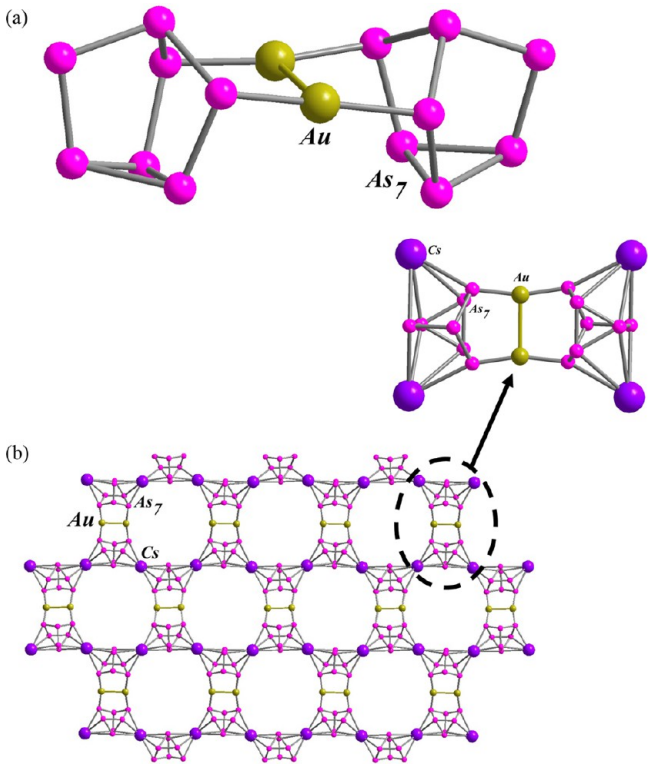

FIGURE 4. (a) Crystal structure of $[Au_2(As_7)_2]^{4-}$, **5**. (b) Two-dimensional distorted honeycomb-like layers of $[Au_2(As_7)_2]^{4-}$ linked by Cs^+ in **7** as viewed along the *a* axis.

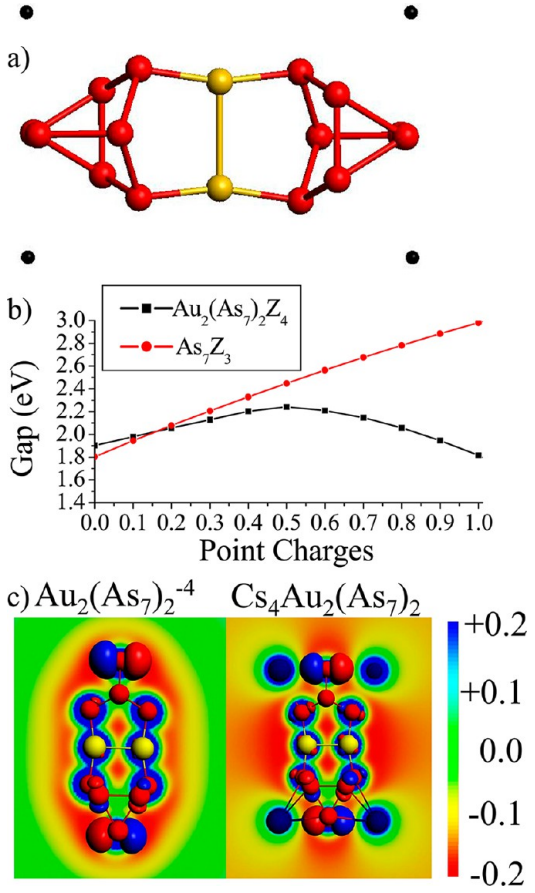

FIGURE 5. (a) The positions of point charges in the cluster model and (b) variation of the band gap energies. (c) The calculated electrostatic potential of $(As_7)_2Au_2^{4-}$ and $Cs_4(As_7)_2Au_2$ (**5** and **7**).

isolated cluster motif? Our hypothesis is that the counterions connected to the clusters generate an internal electric field that alters the band gap energy through modulating orbitals at the band edge in a manner analogous to crystal field theory. To test this idea, we calculated the electronic structure for an isolated $[Au_2(As_7)_2]^{4-}$ cluster (Figure 5a) with four point charges, *z*, placed at the same positions as Cs in the solid. The point charges were varied from 0.0 to +1.0e, and the HOMO–LUMO gap and electronic spectrum were monitored. The HOMO–LUMO gaps increased by 0.34 eV when the point charge was varied from 0 to +0.5e for the gold-linked clusters and then decreased with higher fields. The density of states (DOS) as a function of electric field is shown in Figure S5, Supporting Information. We found that the increase in the HOMO–LUMO gap is caused by stabilization of the HOMO with increasing field, while the LUMO states show little change until $z = +0.6e$. Further increased electric fields reduce the gap because the As–Au mixed states are strongly stabilized to become the LUMO at high field. Similar electric-field-dependent behavior is observed for As_7^{3-} clusters; however, the gap increases monotonically up to 2.98 eV with increasing electric field (Figure 5b). We confirmed this by examining the local electrostatic environment of our cluster models in Figure 5c with the associated HOMO plotted as an isosurface. Figure 5c shows the electrostatic potential of $[(Au_2)(As_7)_2]^{4-}$ and $Cs_4[(Au_2)(As_7)_2]$ because the electric field corresponds to the gradient of the electrostatic potential; a red to blue sequence indicates a stronger electric field. In $[(Au_2)(As_7)_2]^{4-}$, the electrostatic potential falls off gradually from the isolated cluster because no adjacent counterions are present to generate internal electric fields. In contrast, for the case of $Cs_4[(Au_2)(As_7)_2]$, there is a large electric field generated by the Cs counterions, precisely along the path of the HOMO orbital. The band gap energy variation also depends on the precise location of the electric field generated by the counterion and by the charge density of the states near the Fermi energy, so it may not always result in an increase of the band gap energy. These results show that the band gap energies of the 2D ionic solids (**6**–**8**) increase due to the generation of internal electric fields by the adjacent counterions.

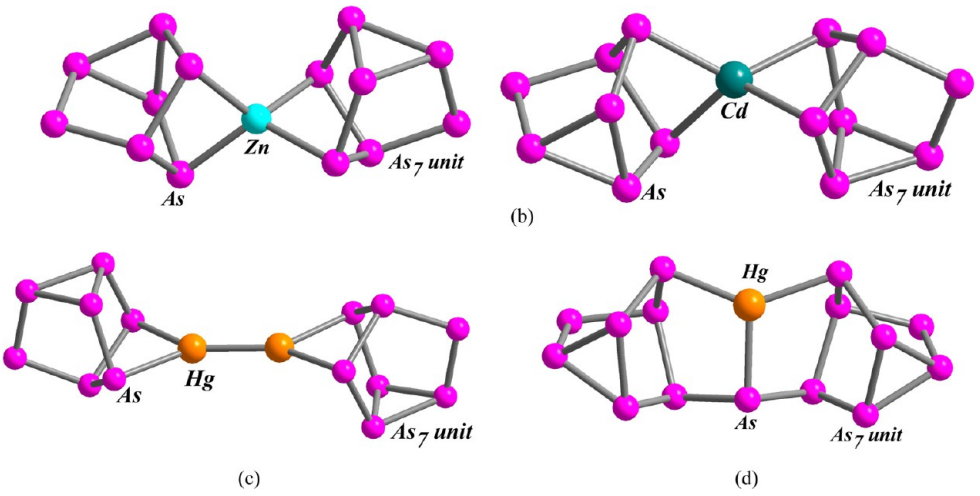

FIGURE 6. Cluster unit of (a) $[K\text{-crypt}]_4[Zn(As_7)_2]\cdot 2en$ (**10**), (b) $[K\text{-crypt}]_4[Cd(As_7)_2]\cdot en$ (**11**), (c) $[K\text{-crypt}]_4[Hg_2(As_7)_2]$ (**12**), and (d) $[K\text{-crypt}]_3[HgAsAs_{14}]$ (**13**). For clarity, [K-crypt] and solvent molecules are not shown.

Band Gap Energy Tuning: Role of Covalent Bonding

Covalently linking clusters offers a third strategy for altering band gap energies. To test this strategy for band gap energy control, we have synthesized a series of cluster-assembled materials in which the building blocks are As_7^{3-} clusters linked by group 12 metals, Zn, Cd, and Hg.[31] We have synthesized 0D assemblies of $[Zn(As_7)_2]^{4-}$ (compound **10**), $[Cd(As_7)_2]^{4-}$ (compound **11**), $[Hg_2(As_7)_2]^{4-}$ (compound **12**), and $[HgAsAs_{14}]^{3-}$ (compound **13**) (Figure 6). The Zn and Cd atoms covalently link the two As_7 clusters as confirmed by the change in the oxidation states of the As_7 clusters decrease from -3 to -2 demonstrating that the clusters have been oxidatively coupled. The band gap energy of $[K\text{-crypt}]_4[Zn(As_7)_2]\cdot 2en$ (compound **10**) was measured to be 1.99 ± 0.05 eV and that of $[K\text{-crypt}]_4[Cd(As_7)_2]\cdot en$ (compound **11**) to be 1.87 ± 0.04 eV (Figure 1 and Table 1).

An examination of the molecular orbital diagrams of $[Cd(As_7)_2]^{4-}$ and $[Zn(As_7)_2]^{4-}$ in Figure 7A,B reveals that the bonding can be rationalized within a cluster orbital picture. In Figure 7, bonding orbitals are indicated by red lines, and antibonding orbitals are indicated by blue lines. In the case of Zn and Cd, the electronic spectrum of As_7^{3-} is maintained after being coupled, except for a few molecular orbitals. One set of deep orbitals of Zn is split into occupied bonding and antiboding orbitals, and a second set of bonding and antibonding orbitals are formed to be the HOMO$-$2 and LUMO+11. The binding energy is calculated to be 2.26 eV, consistent with a covalent bond. The positioning of the HOMO$-$2 bonding orbitals is unusual because the orbital has *b* symmetry requiring that clusters are coupled by a high-energy Zn 4p orbital.

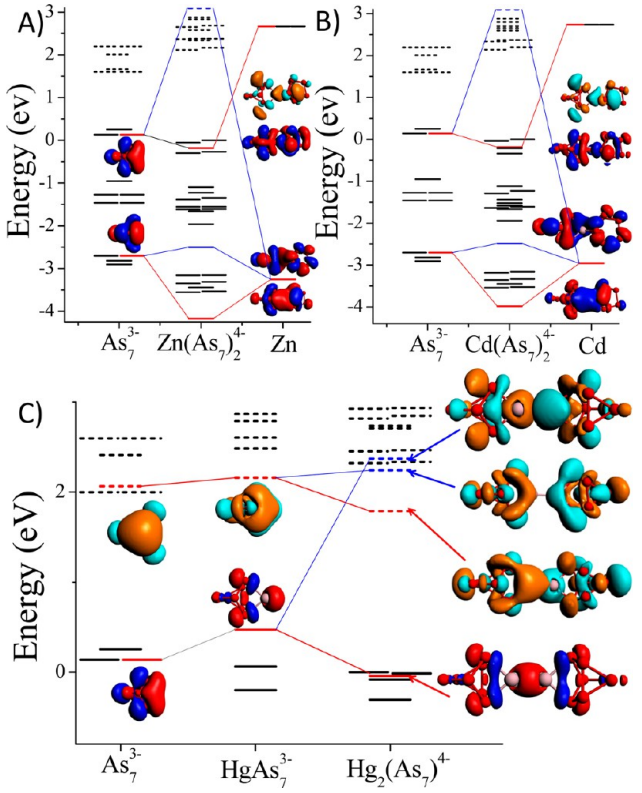

FIGURE 7. Molecular orbital diagram for (A) $[Zn(As_7)_2]^{4-}$, (B) $[Cd(As_7)_2]^{4-}$, and (C) $[Hg_2(As_7)_2]^{4-}$.

The high-energy antibonding orbital has two nodes while having significant contributions from the 4s orbital. A fragment analysis of these orbitals confirms that 67% of the bonding orbital comes from the indicated orbital and 52% of the antibonding orbital comes from this occupied fragment orbital.

To understand the unexpected formation of the Hg$-$Hg bond, we examined the molecular orbital diagram of $[Hg_2(As_7)_2]^{4-}$ (compound **12**). The Hg dimer has a net bond

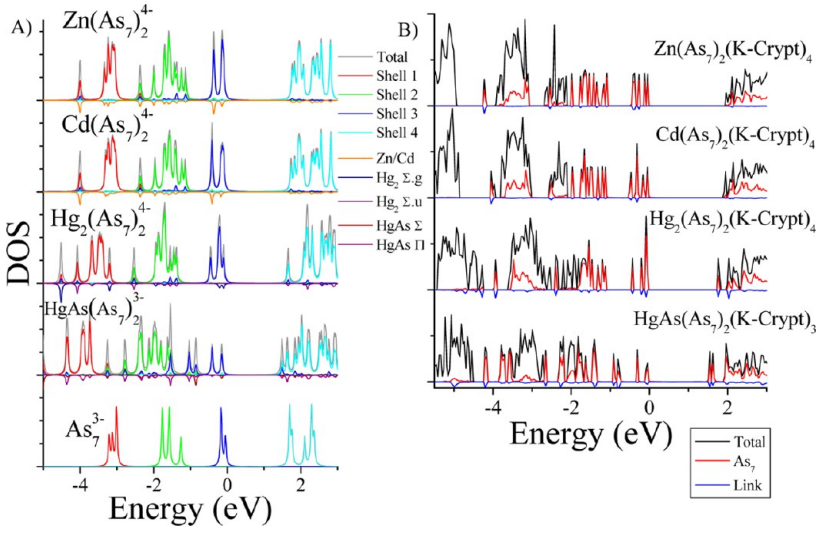

FIGURE 8. (A) The density of states of the cluster models for **10**−**13** and As_7^{3-}. Shells 1−4 represent the projected density of states to the As_7^{3-} cluster molecular orbitals. The negatively plotted states are projected from the linker. (B) The density of states of the periodic calculations for **10**−**13**. Black indicates total density of states, red indicates As_7 states, blue indicates the linker states, and the remaining states are attributed to the crypt.

order of zero because the 6s valence electrons form bonding and antibonding orbitals.[32,33] Hg_2^{2+} is a stable species due to its bond order of one, because the antibonding orbital is unoccupied after oxidation. In compound **12**, the 6s orbital of the Hg atom overlaps with the same HOMO−1 orbital of the As_7^{3-} cluster near the Fermi energy as for the case of Cd and Zn atoms to form the molecular orbital shown in Figure 7c. The $[HgAs_7]^{3-}$ orbitals form bonding and antibonding orbitals when combined, and the antibonding orbital is unfilled, resulting in a net bond order of one with a calculated binding energy of 1.32 eV.[34] Compound **12** is found to have a smaller band gap energy than that of **10** or **11**. This is caused by the splitting of the LUMO level of the $[Hg(As_7)]^{3-}$ intermediate, shown in Figure 7c into a pair of weakly bonding and antibonding orbitals. The LUMO in Figure 7c is stabilized in a weak bonding orbital, reducing the HOMO−LUMO gap energy of the solid. The $[Hg_2(As_7)_2]^{4-}$ is stabilized through oxidative coupling between the cluster−mercury complex, which pushes up the σ antibonding orbital to reduce the oxidation state by two. The measured band gap energy of this compound is 1.67 ± 0.04 eV (Figure 1 and Table 1), ca. 0.32 eV lower than that for compound **10**. To probe the nature of the states marking the occupied and unoccupied bands in the solid, we calculated the electronic structure of the cluster models and periodic structure, and the resulting DOS are shown in Figure 8. Note that unlike compounds **10** and **11**, where the unoccupied band is formed by the electronic states of the crypt, the unoccupied band here is marked by states having significant contributions from the Hg and As_7 cluster orbitals.

Fragment analyses show that the bonding and antibonding orbitals of the composite clusters are built primarily from the molecular orbitals of the initial As_7^{3-} cluster. The oxidative coupling between clusters via Cd, Zn, and Hg are consistent with a "cluster orbital" picture where molecular orbitals of the clusters behave like atomic orbitals in molecular orbital theory.[34]

In compound **13** $[HgAs(As_7)_2]^{3-}$, two As_7 clusters are bound by a Hg−As dimer. The measured band gap energy is the lowest for these covalently linked cluster assemblies. The band gap of 1.62 ± 0.04 eV (Figure 1 and Table 1) is due to broadening of the cluster's electronic band of states from the frontier orbitals.

We have linked the compounds **10** and **11** by Cs and Rb to 3D structures, compounds **14** and **15** respectively, (Figures S6 and S7, Supporting Information) and measured the band gap energy.[31] The increased band gap energy due to the internal electric field generated by the counterion is similar to the Au-linked case.

Band Gap Energy: Linker States Embedded in the Gap

We have synthesized different types of covalently linked clusters where linkers are dimeric. These are $[K\text{-crypt}]_4[Au_2(As_7)_2]$ (**5**), $[K\text{-crypt}]_4[Hg_2(As_7)_2]$ (**12**), and $[K\text{-crypt}]_4[Pd_2(As_7)_2]$ (**16**) (Figures 4a, 6c, and 9a, respectively). The band gap energy of the Pd_2-linked cluster is 1.15 eV, whereas it is 1.67 and 1.69 eV, respectively, for the Hg_2- and Au_2-linked clusters.[35] To probe the much lower band gap energy of the $[Pd_2As_{14}]^{4-}$ motif, we examine the molecular orbital diagram of the As_7^{3-} and $Cs_4[Pd_2As_{14}]$ clusters, analogous to compound **17** (Figure 9b).

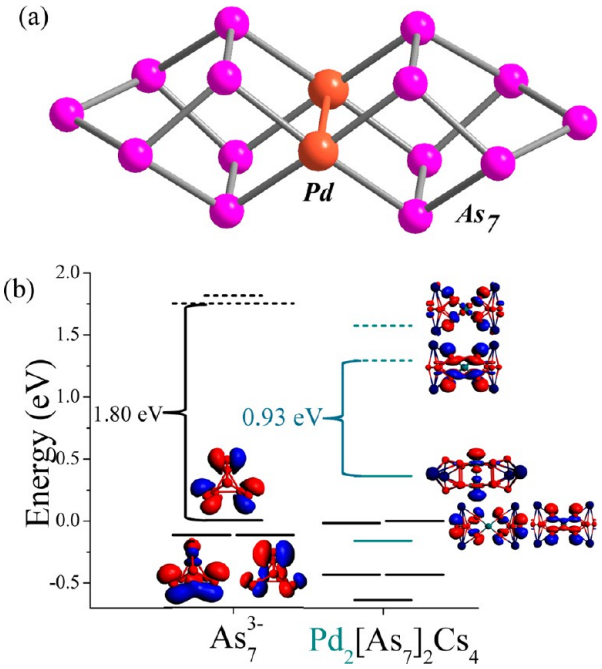

FIGURE 9. (a) The cluster unit of **16**, $[K\text{-crypt}]_4[Pd_2(As_7)_2]\cdot 3en$. (b) Molecular orbital diagram from $[As_7]^{3-}$ and $Pd_2(As_7)_2Cs_4$.

The intrinsic band gap energy of As_7^{3-} is 1.80 eV, so we have aligned the lone pair orbitals from $[Pd_2As_{14}]^{4-}$ with the lone pair orbitals of As_7^{3-}. The lone pair orbitals in As_7^{3-} and $Cs_4[Pd_2As_{14}]$ are both localized on the equatorial atoms and have similar character (Figure 9b). The Pd_2 Σ_u orbital is the HOMO of $Cs_4[Pd_2As_{14}]$ and is 0.36 eV higher than the lone pair orbitals making it a localized orbital embedded in the band gap of As_7^{3-}. This molecular orbital is primarily composed of the $4d_{z^2}$ orbitals of the Pd dimer. The LUMO involves both As_7 and the Pd atoms. This demonstrates that the Pd dimer creates a set of states that are embedded in the band gap of the As_7^{3-} cluster, offering another strategy for controlling the band gap energy.

Band Gap Energy Tuning: Role of Charger Transfer Complex

Charge-transfer complexes are well-known as strong absorbers of visible light, so their incorporation into cluster-assembled materials may affect the optical properties of the materials. We have synthesized and examined the effects of charge transfer on the band gap energy of cluster assemblies from As_7^{3-} bound to one or two $M(CO)_3$ molecules, in which M is one the group VIB elements, Cr, Mo, and W. Our investigations included 0D assemblies of $[As_7Cr(CO)_3]^{3-}$ (**18**), $[(en)Mo(CO)_3As_7(Mo(CO)_3)_2]^{3-}$ (**19**), and $[(en)W(CO)_3As_7(W(CO)_3)_2]^{3-}$ (**20**) and 1D assemblies of $[As_7Cr(CO)_3]^{3-}$ (**21**), $[As_7Mo(CO)_3]^{3-}$ (**22**) and $[As_7W(CO)_3]^{3-}$ (**23**) linked by Cs atoms (Figure 10).[36] To understand the effects of charge-transfer

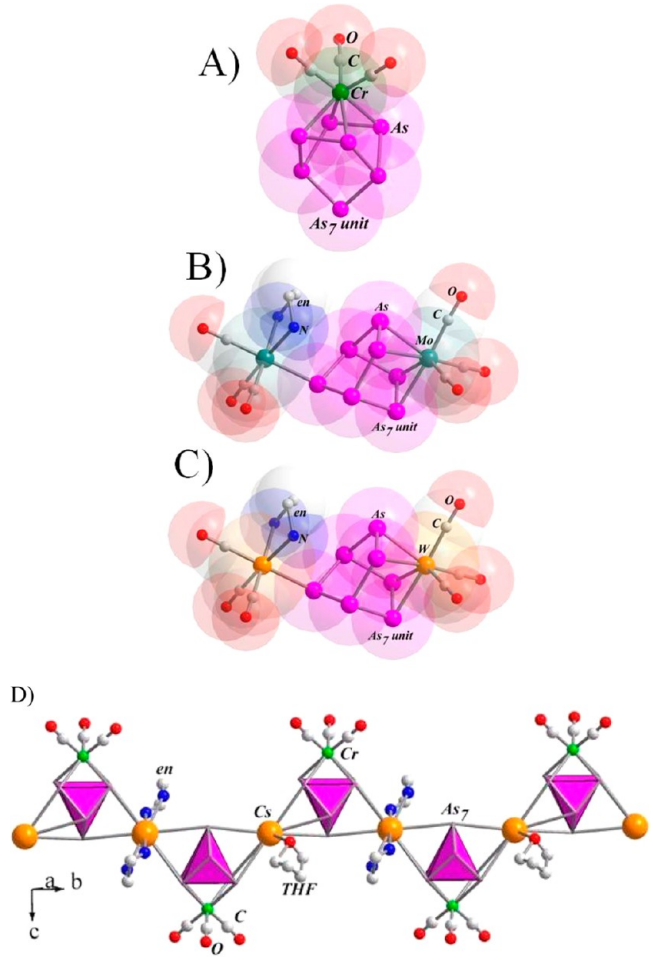

FIGURE 10. X-ray crystallographic structures of (A) $[K\text{-crypt}]_3[As_7Cr(CO)_3]$, **18**; (B) $[K\text{-crypt}]_3[(en)Mo(CO)_3As_7Mo(CO)_3]$, **19**; (C) $[K\text{-crypt}]_3[(en)W(CO)_3WAs_7(CO)_3]$, **20**; and (D) $[K\text{-crypt}]_2[As_7Cr(CO)_3Cs]\cdot en\cdot THF$, **21**. For clarity, K-crypt is not shown.

ligands, we have carried out analyses of the electronic structure. The small variation in the band gap energies of the $[As_7M(CO)_3]^{3-}$ cluster assemblies is due to the small perturbation of the electronic structure of the cluster and the close alignment of the metal carbonyl orbitals and lone pair orbitals of the arsenic cluster. The band gap energy of the isolated $[As_7]^{3-}$ cluster is 1.80 eV, and the variations of the 1D $[As_7M(CO)_3]^{3-}$ clusters and isolated $[As_7Cr(CO)_3]^{3-}$ cluster are all within 0.10 eV of that band gap energy. The bonding between the cluster and metal−carbonyl is due to charge transfer, so the electronic structure of the cluster involves no significant reordering of electronic levels. Furthermore, the lone pair HOMO of the cluster is closely aligned with the HOMO of the metal carbonyl complex so the "valence band edge" of the cluster is unaffected, unlike the Pd dimer case. The LUMO of the metal carbonyl is also quite high in energy, so it does not affect the conduction

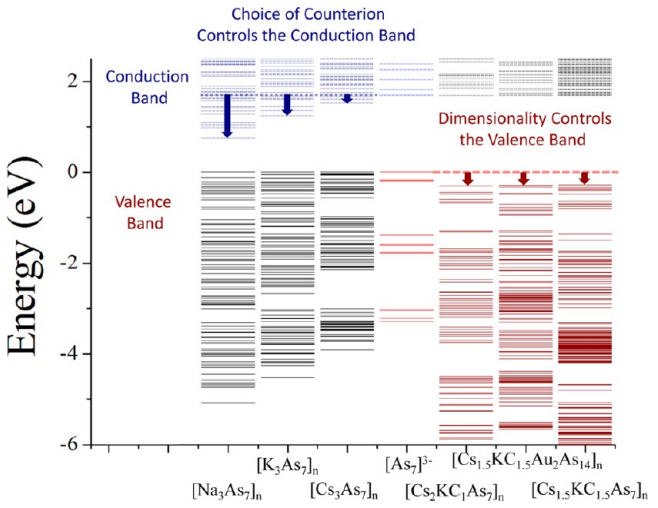

FIGURE 11. The one electron levels at the γ point for Na_3As_7, K_3As_7, Cs_3As_7, the free As_7^{3-} cluster (**5**), **7**, and **3**.

band of the cluster-assembled material. The metal carbonyls cover only one of the three binding sites that alkali metals typically use to link the clusters, so it does enable the formation of 1D chains of clusters linked by alkali atoms. The variations in the band gap energies by these group VIB complexes are quite small, although they do offer a method of controlling dimensionality.

Conclusions

We have presented a comprehensive overview of the nanoscale materials formed from the assembly of bare and linked As_7^{3-} clusters with a variety of countercations. All the assembled materials are semiconductors with energy bands that have little dispersion, indicating minimal direct interaction between cluster-based building blocks. Yet, the band gap of the resulting solids can be varied over a large range from 1.09 to 2.16 eV. Figure 11 demonstrates strategies for changing the positions of both the valence band energy and the conduction band energy. We have found that the identity of the counterion controls the position of the conduction band edge and that starting with the As_7^{3-} building block, the band gap energy decreases as the counterion is switched from Cs to K and Na due to the position of the atomic HOMO. The valence band of the cluster assembly may be controlled through the architecture of the solid, in which internal electric fields generated by the alkali counterion preferentially stabilize the orbitals at the top of the valence band edge. The effect of covalent bonding on the band gap energy has also been investigated using cluster orbital theory. We have studied the effects of additional linkers including palladium, which embed states in the band gap of the cluster causing a decrease in the band gap energy, as well as charge-transfer complexes. These studies have revealed the rich phenomena that emerge as nanoscale clusters are brought together to form hierarchical materials and highlight the promise of nanoscale materials with tunable properties. This work has revealed some of the critical nanoscale design parameters for hard metallic clusters and joins many other efforts to find these critical parameters. For example, in soft nanoclusters including dendimers, the architecture, surface chemistry, size, and shape of dendrimer are found to control the properties and encompass nanoperiodic property patterns for the prediction of dendrimer polymer properties.[37] DNA–nanoparticle superlattices have also been found to have similar critical rules that determine the architecture of the materials.[38] The strategies presented here to control the band gap energy in cluster-assembled materials are fundamental to the goal of advancing the study of clusters and nanoparticles from recipes and techniques to concepts and design rules.

This material is based upon work supported by the U.S. Department of the Army, Army Research Office (AFOSR), through MURI Grant W911NF-06-1-0280. S.N.K. acknowledges support from the AFOSR through MURI Grant No. FA9550-08-1-0400.

Supporting Information. Theoretical calculations, representations of the structures of clusters **3**, **6**, **8**, **14**, and **15**, densities of states for clusters **5**, **7**, and **9**, band structure of **7**, and density of states of an isolated $[Au_2(As_7)_2]^{4-}$ cluster. This material is available free of charge via the Internet at http://pubs.acs.org.

BIOGRAPHICAL INFORMATION

Sukhendu Mandal earned his Ph.D. from the Indian Institute of Science, India. Presently he is pursuing his postdoctoral research at the Pennsylvania State University under the tutelage of Prof. Ayusman Sen. His research interests include cluster-assembled materials, nanoclusters, and catalytic conversion of biomass to targeted liquid fuels.

Arthur C. Reber is a Research Associate Professor of Physics at Virginia Commonwealth University. He received his Ph.D. in Chemistry from the University of Chicago. His research interests include theoretical studies on the reactivity and electronic properties of clusters and nanoparticles.

Meichun Qian is a Research Assistant Professor of Physics at Virginia Commonwealth University. He received his Ph.D. in Physics from Chinese Academy of Science. His research interests include theoretical studies of magnetic properties and cluster-assembled materials.

Paul S. Weiss holds the Fred Kavli Chair in NanoSystems Sciences, is Director of the California NanoSystems Institute, and is a Distinguished Professor of Chemistry & Biochemistry and of Materials Science & Engineering at the University of California,

Los Angeles. He is the founding editor-in-chief of *ACS Nano*. He is a Fellow of the American Association for the Advancement of Science, the American Chemical Society, the American Physical Society, and the American Vacuum Society, and an Honorary Fellow of the Chinese Chemical Society. His research focuses on understanding and controlling single-molecule/assembly structure, function, and spectra, precisely assembled materials, and chemical patterning at all scales.

Shiv N. Khanna is a Commonwealth Professor of Physics at Virginia Commonwealth University. He is a Fellow of the American Association for the Advancement of Science and the American Physical Society. His research interests are involved in theoretical studies of the electronic structure and magnetic and catalytic properties of atomic clusters, cluster assemblies, and nanoscale materials. He (with colleagues) proposed the concept of "superatoms" that extend the Periodic Table to a third dimension.

Ayusman Sen received his Ph.D. from the University of Chicago. Following a year of postdoctoral work at the California Institute of Technology, he joined the Chemistry Department of the Pennsylvania State University, where is currently a Distinguished Professor. He is a Fellow of the American Association for the Advancement of Science. His research interests encompass catalysis, organometallic and polymer chemistry, and nanotechnology.

FOOTNOTES

*Corresponding authors. E-mail addresses: snkhanna@vcu.edu; asen@chem.psu.edu; psw@cnsi.ucla.edu.

The authors declare no competing financial interest.

[⊥]S.M. and A.C.R. made equal contributions to this work.

[∥]Present address, S.M.: School of Chemistry, Indian Institute of Science Education and Research, Thiruvananthapuram, Kerala 695016, India.

REFERENCES

1 Claridge, S. A.; Castleman, A. W., Jr.; Khanna, S. N.; Murray, C. B.; Sen, A.; Weiss, P. S. Cluster-Assembled Materials. *ACS Nano* **2009**, *3*, 244–255.

2 Scharfe, S.; Kraus, F.; Stegmaier, S.; Schier, A.; Fässler, T. F. Zintl Ions, Cage Compounds, and Intermetalloid Clusters of Group 14 and Group 15 Elements. *Angew. Chem., Int. Ed.* **2011**, *50*, 3630–3670 and references therein.

3 Murray, C. B.; Norris, D. J.; Bawendi, M. G. Synthesis and Characterization of Nearly Monodisperse CdE (E = Sulfur, Selenium, Tellurium) Semiconductor Nanocrystallites. *J. Am. Chem. Soc.* **1993**, *115*, 8706–8715.

4 Huynh, W. U.; Dittmer, J. J.; Alivisatos, A. P. Hybrid Nanorod-Polymer Solar Cells. *Science* **2002**, *295*, 2425–2427.

5 Warburton, R. J.; Schaflein, C.; Haft, D.; Bickel, F.; Lorke, A.; Karrai, K.; Garcia, J. M.; Schoenfeld, W.; Petroff, P. M. Optical Emission from a Charge-Tunable Quantum Ring. *Nature* **2000**, *405*, 926–929.

6 Armatas, G. S.; Kanatzidis, M. G. Hexagonal Mesoporous Germanium. *Science* **2006**, *313*, 817–820.

7 Guloy, A. M.; Ramlau, R.; Tang, Z.; Schnelle, W.; Baitinger, M.; Grin, Y. A. Guest-Free Germanium Clathrate. *Nature* **2006**, *443*, 320–323.

8 Sun, D.; Riley, A. E.; Cadby, A. J.; Richman, E. K.; Korlann, S. D.; Tolbert, S. H. Hexagonal Nanoporous Germinum through Surfactant-Driven Self-Assembly of Zintl Clusters. *Nature* **2006**, *441*, 1126–1130.

9 Korlann, S. D.; Riley, A. E.; Mun, B. S.; Tolbert, S. H. Chemical Tuning of the Electronic Properties of Nanostructured Semiconductor Films Formed through Surfactant Templating of Zintl Cluster. *J. Phys. Chem. C* **2009**, *113*, 7697–7705.

10 Riley, A. E.; Korlann, S. D.; Richman, E. K.; Tolbert, S. H. Synthesis of Semiconducting Thin Films with Nanometer-Scale Periodicity by Solution-Phase Coassembly of Zintl Clusters with Surfactants. *Angew. Chem., Int. Ed.* **2006**, *45*, 235–241.

11 Sanchez, A.; Abbet, S.; Heiz, U.; Schneider, W.-D.; Häkkinen, H.; Barnett, R. N.; Landman, U. When Gold Is Not Noble: Nanoscale Gold Catalysts. *J. Phys. Chem. A* **1999**, *103*, 9573–9578.

12 Wang, Y.; Yamachika, R.; Wachowiak, A.; Grobis, M.; Crommie, M. Tuning Fulleride Electronic Structure and Molecular Ordering via Variable Layer Index. *Nat. Mater.* **2008**, *7*, 194–197.

13 Castleman, A. W., Jr.; Khanna, S. N.; Sen, A.; Reber, A. C.; Qian, M.; Davis, K. M.; Peppernick, S. J.; Ugrinov, A.; Merritt, M. D. From Designer Clusters to Synthetic Crystalline Nanoassemblies. *Nano Lett.* **2007**, *7*, 2734–2741.

14 Ugrinov, A.; Sen, A.; Reber, A. C.; Qian, M.; Khanna, S. N. $[Te_2As_2]^{2-}$: A Planar Motif with "Conflicting" Aromaticity. *J. Am. Chem. Soc.* **2008**, *130*, 782–783.

15 Bera, T. K.; Jang, J. I.; Ketterson, J. B.; Kanatzidis, M. G. Strong Second Harmonic Generation from the Tantalum Thioarsenates $A_3Ta_2AsS_{11}$ (A = K and Rb). *J. Am. Chem. Soc.* **2009**, *131*, 75–77.

16 Reber, A. C.; Khanna, S. N.; Castleman, A. W., Jr. Superatom Compounds, Clusters, and Assemblies: Ultra Alkali Motifs and Architectures. *J. Am. Chem. Soc.* **2007**, *129*, 10189–10194.

17 Mudring, A.-V.; Corbett, J. D. Importance of Cations in the Properties of Zintl Phases: The Electronic Structure and Bonding in Metallic Na_6TlSb_4. *Inorg. Chem.* **2005**, *44*, 5636–5640.

18 Mudring, A. V.; Corbett, J. D. Unusual Electronic and Bonding Properties of the Zintl Phase Ca_5Ge_3 and Related Compounds. A Theoretical Analysis. *J. Am. Chem. Soc.* **2004**, *126*, 5277–5281.

19 Castleman, A. W., Jr.; Khanna, S. N. Clusters, Superatoms, and Building Blocks of New Materials. *J. Phys. Chem. C* **2009**, *113*, 2664–2675.

20 Pelaz, B.; Jaber, S.; Jimenez de Aberasturi, D.; Wulf, V.; Aida, T.; de la Fuente, J. M.; Feldmann, J.; Gaub, H. E.; Josephson, L.; Kagan, C. R.; Kotov, N. A.; Liz-Marzán, L. M.; Mattoussi, H.; Mulvaney, P.; Murray, C. B.; Rogach, A. L.; Weiss, P. S.; Willner, I.; Parak, W. J. The State of Nanoparticle-Based Nanoscience and Biotechnology: Progress, Promises, and Challenges. *ACS Nano* **2012**, *6*, 8468–8483.

21 Zintl, E. Intermetallische Verbindungen. *Angew. Chem.* **1939**, *52*, 1–6.

22 *Chemistry, Structure, and Bonding of Zintl Phases and Ions*; Kauzlarich, S. M., Ed.; VCH: New York, 1996.

23 Qian, M.; Reber, A. C.; Ugrinov, A.; Chaki, N. K.; Mandal, S.; Saavedra, H. M.; Khanna, S. N.; Sen, A.; Weiss, P. S. Cluster-Assembled Materials: Towards Nanomaterials with Precise Control over Properties. *ACS Nano* **2010**, *4*, 235–240.

24 Kubelka, P. New Contributions to the Optics of Intensely Light Scattering Materials. I. *J. Opt. Soc. Am.* **1948**, *38*, 448–457.

25 Kubelka, P. New Contributions to the Optics of Intensely Light Scattering Materials. II. Non-Homogeneous Layers. *J. Opt. Soc. Am.* **1954**, *44*, 330–335.

26 Murphy, A. B. Modified Kubelka-Munk Model for Calculation of the Reflectance of Coatings with Optically-Rough Surfaces. *J. Phys. D: Appl. Phys.* **2006**, *39*, 3571–3581.

27 Tauc, J.; Grigorocici, R.; Vacnu, A. Optical Properties and Electronic Structure of Amorphous Germanium. *Phys. Status Solidi* **1966**, *15*, 627–637.

28 Tauc, J. In *The Optical Properties of Solids*; Abeles, F., Ed.; North-Holland: Amsterdam, The Netherlands, 1972.

29 Laidani, N.; Bartali, R.; Gottardi, G.; Anderle, M. Optical Absorption Parameters of Amorphous Carbon Films from Forouhi-Bloomer and Tauc-Lorentz Models: A Comparative Study. *J. Phys.: Condens. Matter* **2008**, *20*, No. 015216.

30 Chaki, N. K.; Mandal, S.; Reber, A. C.; Qian, M.; Saavedra, H. M.; Weiss, P. S.; Khanna, S. N.; Sen, A. Controlling Band Gap Energies in Cluster-Assembled Ionic Solids through Internal Electric Fields. *ACS Nano* **2010**, *4*, 5813–5818.

31 Mandal, S.; Reber, A. C.; Qian, M.; Liu, R.; Saavedra, H. M.; Sen, S.; Weiss, P. S.; Khanna, S. N.; Sen, A. Synthesis, Structure and Band Gap Energy of Covalently Linked Cluster-Assembled Materials. *Dalton Trans.* **2012**, *41*, 12365–12377.

32 Epstein, L. F.; Powers, M. D. Liquid Metals. I. The Viscosity of Mercury Vapor and the Potential Function for Mercury. *J. Phys. Chem.* **1953**, *57*, 336–341.

33 Haberland, H.; von Issendorff, B.; Yufeng, J.; Kolar, T.; Thanner, G. Ground State and Response Properties of Mercury Clusters. *Z. Phys. D* **1993**, *26*, 8–12.

34 Mandal, S.; Reber, A. C.; Qian, M.; Liu, R.; Saavedra, H. M.; Sen, S.; Weiss, P. S.; Khanna, S. N.; Sen, A. On the Stability of an Unsupported Mercury-Mercury Bond Linking Group 15 Zintl Clusters. *Dalton Trans.* **2012**, *41*, 5454–5457.

35 Reber, A. C.; Mandal, S.; Qian, M.; Saavedra, H. M.; Weiss, P. S.; Khanna, S. N.; Sen, A. Palladium in the Gap: Cluster Assemblies with Band Edges Localized on Linkers. *J. Phys. Chem. C* **2012**, *116*, 10207–10214.

36 Mandal, S.; Qian, M.; Reber, A. C.; Saavedra, H. M.; Weiss, P. S.; Khanna, S. N.; Sen, A. $[As_7M(CO)_3]^{3-}$ M = Cr, Mo, W: Bonding and Electronic Structure of Cluster Assemblies with Metal Carbonyls. *J. Phys. Chem. C* **2011**, *115*, 23704–23710.

37 Tomalia, D. A. Dendritic Effects: Dependency of Dendritic Nano-Periodic Property Patterns on Critical Nanoscale Design Parameters (CNDPs). *New. J. Chem.* **2012**, *26*, 246–281.

38 Macfarlane, R. J.; Lee, B.; Jones, M. R.; Harris, N.; Schatz, G. C.; Mirkin, C. A. Nanoparticle Superlattice Engineering with DNA. *Science* **2011**, *334*, 204–208.